Geophysical Research Letters

RESEARCH LETTER
10.1029/2019GL084202

Key Points:

- Strong EMIC waves were observed by Van Allen Probe A in association with phase space density dips over the similar L shell extent
- FIREBIRD-II observed electron precipitation from ~250 keV up to ~1 MeV over the similar L shell extent of EMIC waves but at a later MLT
- Quasi-linear theory predicts efficient precipitation at > 0.8–1 MeV but requires other mechanisms to explain the subrelativistic one

Supporting Information:

- Supporting Information S1
- Figure S1
- Figure S2
- Figure S3

Correspondence to:
L. Capannolo and W. Li,
luisacap@bu.edu;
wenli77@bu.edu

Citation:
Capannolo, L., Li, W., Ma, Q., Chen, L., Shen, X.-C., Spence, H. E., et al. (2019). Direct observation of subrelativistic electron precipitation potentially driven by EMIC waves. *Geophysical Research Letters*, *46*, 12,711–12,721. https://doi.org/10.1029/2019GL084202

Received 21 JUN 2019
Accepted 8 NOV 2019
Accepted article online 15 NOV 2019
Published online 25 NOV 2019
Corrected 16 DEC 2019

This article was corrected on 16 DEC 2019. Please see the end of the full text for details.

Direct Observation of Subrelativistic Electron Precipitation Potentially Driven by EMIC Waves

L. Capannolo[1], W. Li[1], Q. Ma[1,2], L. Chen[3], X.-C. Shen[1], H. E. Spence[4], J. Sample[5], A. Johnson[5], M. Shumko[5], D. M. Klumpar[5], and R. J. Redmon[6]

[1]Center for Space Physics, Boston University, Boston, MA, USA, [2]Department of Atmospheric and Oceanic Sciences, University of California, Los Angeles, CA, USA, [3]William B. Hanson Center for Space Sciences, University of Texas at Dallas, Richardson, TX, USA, [4]Institute for the Study of Earth, Oceans, and Space, University of New Hampshire, Durham, NH, USA, [5]Department of Physics, Montana State University, Bozeman, MT, USA, [6]Cooperative Institute for Research in Environmental Sciences, University of Colorado Boulder, Boulder, CO, USA

Abstract Electromagnetic ion cyclotron (EMIC) waves are known to typically cause electron losses into Earth's upper atmosphere at >~1 MeV, while the minimum energy of electrons subject to efficient EMIC-driven precipitation loss is unresolved. This letter reports electron precipitation from subrelativistic energies of ~250 keV up to ~1 MeV observed by the Focused Investigations of Relativistic Electron Burst Intensity, Range and Dynamics (FIREBIRD-II) CubeSats, while two Polar Operational Environmental Satellites (POES) observed proton precipitation nearby. Van Allen Probe A detected EMIC waves (~0.7–2.0 nT) over the similar L shell extent of electron precipitation observed by FIREBIRD-II, albeit with a ~1.6 magnetic local time (MLT) difference. Although plasmaspheric hiss and magnetosonic waves were also observed, quasi-linear calculations indicate that EMIC waves were the most efficient in driving the electron precipitation. Quasi-linear theory predicts efficient precipitation at >0.8–1 MeV (due to H-band EMIC waves), suggesting that other mechanisms are required to explain the observed subrelativistic electron precipitation.

Plain Language Summary Plasma waves in the Earth's magnetosphere can alter the trajectory of particles traveling along geomagnetic field lines. Specifically, electromagnetic ion cyclotron (EMIC) waves can interact with both electrons and protons and cause them to fall into the upper atmosphere of Earth. From past studies and theories, it is known that EMIC waves drive precipitation of ultrarelativistic (>~MeV) electrons and tens to hundreds of keV protons. Such electron precipitation can lead to atmospheric changes and potentially aid ozone depletion. In this work, we show a direct observation of electron precipitation from ~250 keV up to ~1 MeV, potentially driven by EMIC waves using multipoint measurements primarily from a CubeSat mission (FIREBIRD-II) and Van Allen Probes. Quasi-linear calculations indicate that EMIC waves are efficient in driving the electron precipitation at >0.8–1 MeV, but other mechanisms are needed to explain the observed electron precipitation down to ~250 keV. Our study also highlights the capabilities of FIREBIRD-II studying not only microbursts, but also other precipitation patterns (e.g., driven by EMIC waves).

1. Introduction

Electromagnetic ion cyclotron (EMIC) waves occur in the Earth's magnetosphere, typically below the hydrogen, helium, and oxygen ion gyrofrequencies (f_{cH}, f_{cHe}, and f_{cO}), with frequencies of 0.1–5 Hz (Erlandson & Ukhorskiy, 2001; Fraser et al., 2010). As EMIC waves mainly propagate along geomagnetic field lines, they are observable at ground as Pc1–Pc2 waves (Engebretson et al., 2008, 2018), although they can spread from the original source region due to ionospheric ducting (Engebretson et al., 2015; Kim et al., 2010). EMIC waves are generally excited during enhanced geomagnetic activity, when ring current ions are injected from the magnetotail (Fraser et al., 2010; Jordanova et al., 2008), thus occur more frequently from postnoon to dusk in the inner magnetosphere (Allen et al., 2016; Blum et al., 2017; Min et al., 2012).

EMIC waves scatter ~MeV electrons and ~10s–100s keV protons into the loss cone via cyclotron resonance, potentially leading to losses of radiation belt electrons and ring current ions (Cao et al., 2016; Jordanova et al., 2008; Jordanova & Miyoshi, 2005; Li et al., 2007; Meredith et al., 2014; Summers et al., 2017;

Summers & Thorne, 2003). While precipitating protons can produce proton aurora (Miyoshi et al., 2008; Yuan et al., 2010), ~MeV electrons can interact with atmospheric nitrogen and hydrogen oxides, leading to ozone reduction (e.g., Meraner & Schmidt, 2018). The efficacy of EMIC waves in scattering MeV electrons and ring current protons has been confirmed in multiple studies, both observationally and theoretically (Blum et al., 2015; Capannolo et al., 2018, 2019; Hirai et al., 2018; Qin et al., 2018, 2019; Shekhar et al., 2017; Woodger et al., 2018; Yuan et al., 2018). However, the techniques and the satellites used have limitations that still leave a few open questions, for example, on the minimum energy of electrons (E_{min}) that can be scattered into the loss cone. Many previous studies indicate that only ~MeV electrons can be scattered by EMIC waves (Chen et al., 2011; Meredith et al., 2003; Ni et al., 2015; Summers & Thorne, 2003). However, more recent studies, such as nonresonant interactions, suggest that the electron precipitation can extend to sub–MeV energies (Chen et al., 2016). Although some studies reported sub–MeV electron precipitation events potentially driven by EMIC waves (Capannolo et al., 2019; Clilverd et al., 2015; Hendry et al., 2017), a direct observation of subrelativistic electron precipitation due to EMIC waves is still limited. The often used National Oceanic and Atmospheric Administration (NOAA) Polar Operational Environmental Satellites (POES), in fact, only detect electrons in integral energy channels. Therefore, even if precipitation in the >300-keV channel occurred (Capannolo et al., 2019; Hendry et al., 2017), it is difficult to determine E_{min} of the precipitating electrons, unless by using some assumptions and modeling. In addition, proton contamination often affects POES lower-energy channels and, despite removal (e.g., Peck et al., 2015), precipitation can still sometimes be misinterpreted. Among the satellites available so far, the Focused Investigations of Relativistic Electron Burst Intensity, Range and Dynamics (FIREBIRD-II) CubeSats provide an excellent opportunity to analyze E_{min} of precipitating electrons driven by EMIC waves, given their high energy resolution.

Our study focuses on the electron precipitation (from ~250 keV to ~1 MeV) observed by FIREBIRD-II CubeSats. By taking full advantage of available multipoint measurements, we discuss several indicators suggesting that the subrelativistic electron precipitation is potentially caused by EMIC waves. We follow up the observations with quasi-linear modeling to determine if EMIC waves can drive the observed electron precipitation.

2. Observations

Figures 1a and 1b show the electron observations by FIREBIRD-II (hereafter simply FIREBIRD) on 9 July 2017 over 2–3 UT. The twin FIREBIRD 1.5 U CubeSats (Flight Units, FU) were launched on 31 January 2015 as a continuation of the original FIREBIRD mission, operational from December 2013 to June 2014 (Klumpar et al., 2015; Spence et al., 2012). Previous studies have been successful in investigating characteristics and spatial/temporal structure of electron microbursts (Breneman et al., 2017; Crew et al., 2016; Shumko et al., 2018). However, FIREBIRD has also the potential of studying other precipitation patterns, such as EMIC-driven precipitation as shown in this letter. The two units measure electron precipitation in five differential channels and one integral channel, along a 632 × 433-km orbit with 99° inclination and a ~90-min orbital period. Count rates are converted to differential fluxes at the central (lowest) energy for the differential (integral) energy channels using a GEometry And Tracking (GEANT4) simulation. GEANT4 also shows minimal proton contamination, significant only for > MeV protons. Figures 1i and 1ii present the L shell and magnetic local time (MLT) values (solid lines) of FU4 and FU3 for different magnetic field models (T89 in black (Tsyganenko, 1989) and T05 in blue (Tsyganenko & Sitnov, 2005)). The MLT values for T89 and T05 overlap. Panels 1iii show the high-resolution electron flux color coded with energy. FU4 and FU3 crossed the same region within ~11 min and both observed electron precipitation across all energy channels, indicating that it occurred not only for relativistic electrons but also for subrelativistic ones, at least down to ~250 keV. While FIREBIRD does not have a fixed pointing direction, it is reasonable to assume that the observations in this case correspond to precipitating electrons rather than trapped ones, given the FIREBIRD location West of the South Atlantic Anomaly (lat~−66°, lon~−148°, within a region of quasi-trapped particles as in Greeley et al. (2019), Figure 1), and no other electron or proton enhancements west of FIREBIRD (NOAA-19 at ~2:30 UT, MLT ~ 13–14, not shown), which excludes the presence of drifting electrons from west.

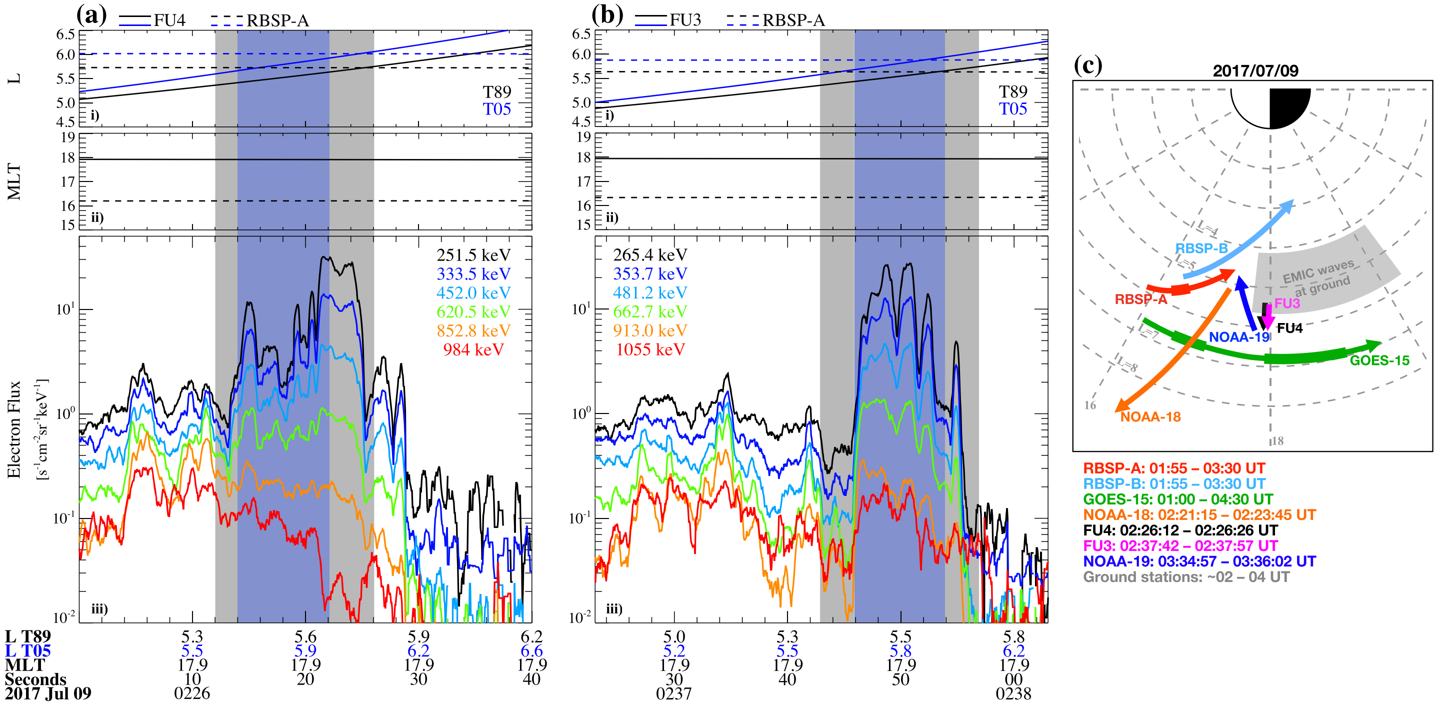

Figure 1. FIREBIRD-II observations: FU4 (a) and FU3 (b). (i) L shell, (ii) MLT for FU (solid line) and RBSP-A (dashed line): The black (blue) line indicates the values from the T89 (T05) model, as marked in the *x* axes; (iii) electron fluxes color coded with energy channels from the 50-ms high-resolution data, smoothed for better visualization with a 450-ms window. The gray (blue) shaded block shows the T89 (T05) L shell extent of EMIC waves observed by RBSP-A mapped onto the FIREBIRD trajectories. The *x* axes values refer only to the FIREBIRD units. (c) Color-coded trajectories of the satellites observing the event and location of the collection of ground-based stations observing EMIC waves (gray region) mapped onto the L (T89)-MLT plane. Thicker lines on RBSP-A and GOES-15 `indicate the intervals when EMIC waves were detected (~02:30–02:55 UT, and ~01:30–2:00 UT and 3:00–04:10 UT). The legend shows the time intervals of the trajectories plotted; for the POES satellites, the time stamps indicate when proton precipitation was observed; for FU, the time stamps refer to the UT intervals of the gray blocks in (a) and (b).

Figure 1c shows a schematic overview of the trajectories of the satellites used in this study and the collection of the ground-based observations onto the L-MLT plane. Both FU were in close L shell conjunction with Van Allen Probe A (RBSP-A, dashed lines, Figures 1i and 1ii) at ~02:26:26 and ~02:37:54 UT respectively, with ΔMLT ~ 1.6. Observations by RBSP-A (Figure 2) are useful to understand the driver of the precipitation observed by FIREBIRD. Van Allen Probes have orbital period, perigee and apogee of ~9 hr, ~600 km, and ~6 R_E, respectively (Mauk et al., 2013). The event occurred during a strong substorm (AL ~ −900 nT, Figure 2a) but over a nonstorm period (Dst > −20 nT). Over 02:00–03:30 UT, RBSP-A was traveling inbound within the plasmasphere (density ~ 130 cm^{-3}, Figure 2b, inferred from the upper hybrid resonance frequency observed by the High-Frequency Receiver, HFR; Kurth et al., 2015) on the dusk side. We use Electric and Magnetic Field Instrument Suite and Integrated Science (EMFISIS, Kletzing et al., 2013) to analyze the magnetospheric wave properties over 10 Hz to 400 kHz. Figures 2c–2f show the enhancement of magnetosonic (MS) waves (~37 pT) with frequency below the lower hybrid resonance frequency (f_{LH}) identified based on their linear polarization (ellipticity ~ 0, Figure 2e) and oblique propagation (Figure 2f). Moreover, very weak hiss emissions (~8 pT) were observed inside the plasmasphere. EMIC waves (from the triaxial fluxgate magnetometer) were observed simultaneously (Figure 2g), both in the helium and hydrogen band over ~02:30–02:55 UT. RBSP-B, traveling at lower L shells (~3.0–5.2), did not observe EMIC waves. Proton flux (Figure 2h, from the Helium, Oxygen, Proton, Electron Mass Spectrometer, HOPE in the Energetic Particle, Composition, and Thermal Plasma Suite, ECT; Funsten et al., 2013; Spence et al., 2013) showed injection of ~ 10s keV protons from the magnetotail, associated with enhanced EMIC wave activity. The L shell extent of EMIC waves observed by RBSP-A was L ~ 5.4–5.7 for T89 (L ~ 5.7–5.9 for T05), projected along the FIREBIRD trajectories as a gray (blue) vertical colored block in Panels 1iii. The strongest electron precipitation observed by FIREBIRD was consistent with the L shell extent and location of the EMIC waves observed by RBSP-A, although the two spacecraft were ~1.6 MLT apart. In addition, given that the

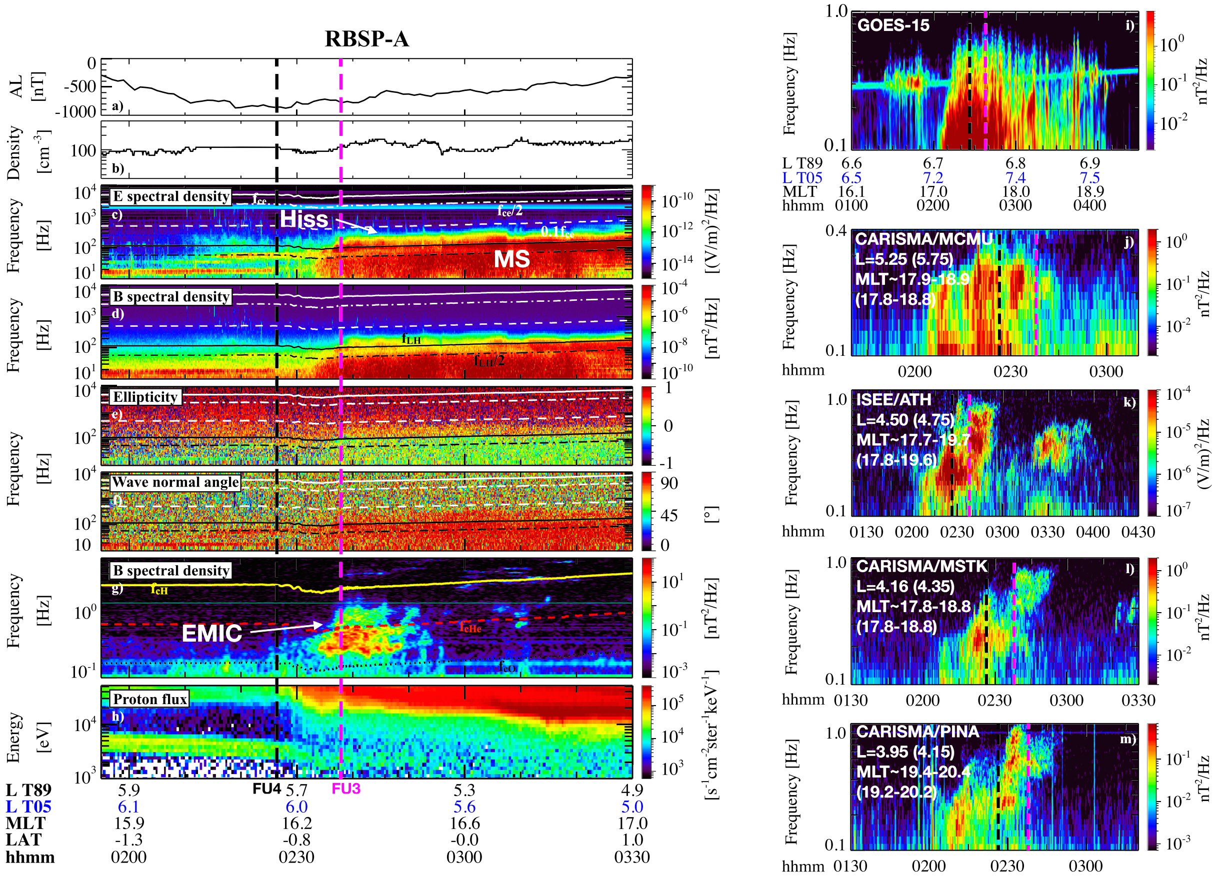

Figure 2. Overview of wave observations. From RBSP-A: (a) AL index, (b) total electron density, (c and d) frequency-time spectrogram of electric and magnetic spectral density, (e) ellipticity, (f) wave normal angle, (g) spectrogram of magnetic spectral density from MAG, and (h) proton flux from HOPE. (i) GOES-15 EMIC wave observations. EMIC wave observations at ground-based stations: (j) CARISMA/MCMU, (k) ISEE/ATH, (l) CARISMA/MSTK, and (m) CARISMA/PINA, with indicated L and MLT values from IGRF and T89 (in parentheses). The vertical dashed lines indicate the UT of magnetic conjunction with FU4 (black) and FU3 (magenta). L T89 (black) and L T05 (blue) on the *x* axes indicate the L shell values from the T89 and T05 magnetic field model, respectively.

electron flux outside this L shell extent was still larger than the background level, especially at lower L shells, precipitation may have occurred even beyond this region, probably due to a larger extent of EMIC waves than that observed by RBSP-A alone. In fact, GOES-15 (part of the Geostationary Operational Environmental Satellite constellation) also recorded EMIC wave activity near dusk over L shells of ~6.5–7.5 (Figure 2i) before 2 UT and after ~3 UT (the waves observed over 2–3 UT are probably relevant to other ultralow frequency waves (ULF), such as Pi2). Additionally, EMIC wave activity was recorded at ground, as shown in Figures 2j–2m by the stations MCMU, MSTK, and PINA in the Canadian Array for Realtime Investigations of Magnetic Activity (CARISMA, Mann et al., 2008) and ATH magnetometer, part of the Institute for Space-Earth Environmental Research (ISEE). The extent of these observations is likely relevant to ionospheric ducting (Kim et al., 2010). The collection of such ground magnetometer observations (L ~ 4.1–5.3, MLT ~ 17.7–20.4), together with the observations from RBSP-A and GOES-15, showed that EMIC wave activity occurred over a rather broad region, although these observations are not necessarily relevant to the same EMIC waves stretching in L and MLT.

As mentioned in section 1, EMIC waves typically scatter not only electrons but also ~ 10s keV protons. Since FIREBIRD only provides electron measurements, we take advantage of the NOAA/POES constellation to investigate the evidence of proton precipitation. NOAA-18 and NOAA-19 (Figure S1 in the supporting information) were traveling in a similar L-MLT region to RBSP-A and FIREBIRD (Figure 1c), and both observed proton precipitation at energies over 10s–100s keV (more details in the Supporting Information), roughly consistent with the L shell extent and location of EMIC waves observed by RBSP-A. These observations, together with ground-based measurements, provide additional evidence that EMIC waves were active longitudinally and driving scattering at MLTs between RBSP-A and FIREBIRD locations.

3. Evolution of Electron PSD

Electron phase space density (PSD) evolution provides key information on the nonadiabatic radiation belt electron dynamics to evaluate whether the EMIC waves played a significant role in electron loss in this event. Figure 3 shows the PSD as a function of L* (T05, Tsyganenko & Sitnov, 2005) for fixed values of the first (μ) and second (K) adiabatic invariants, calculated using the method by Chen et al. (2006) over the interval including RBSP-A EMIC wave observations (00–05 UT). PSD showed decreases from the first pass (black to dark blue lines) to the second one (cyan to green) within a narrow region of L*~4.8–5.1 (highlighted by gray blocks), with more evident PSD dips for increasing values of μ and K. For example, at low μ and K in Figure 3a (~60° pitch angle and energy ~300 keV, at L * ~4.8–5.1), even though the electron PSD dropout was present, it was not as clear as that at higher μ in Figure 3g, where the electron energy is ~1 MeV. Similarly, the PSD dip in Figure 3a is less evident than that in Figure 3c where higher values of K correspond to lower pitch angles (~30°). These PSD dips that occurred within such a spatially narrow region and deepened with increasing values of μ and K are neither the signature of magnetopause shadowing nor that of outward radial diffusion loss, instead are consistent with local pitch angle scattering losses caused by EMIC waves (Shprits et al., 2017; Su et al., 2016; Xiang et al., 2017). EMIC waves are known to be more efficient in scattering electrons at higher energies and low-intermediate pitch angles (Jordanova et al., 2008; Meredith et al., 2003; Usanova et al., 2014), which accounts for the PSD evolution trends as those in Figure 3. Reasonably, the region where these PSD minima occurred for this event overall agrees with the location, spatial extent (L * ~4.7–4.9), and UT (~2–3 UT) of EMIC waves observed by RBSP-A (and also electron precipitation observed by FIREBIRD), suggesting that these waves are important in this event for depleting the outer radiation belt electrons through scattering them into the loss cone. Since the dips were already visible at relatively low values of μ (~200 MeV/G), such a loss was effective at subrelativistic energies as well.

4. Quantifying Electron Precipitation Using Quasi-Linear Theory

The location of wave observations from RBSP-A and at ground, the associated electron precipitation, as well as the results of the PSD analysis, suggest that EMIC waves potentially drove such electron precipitation. Among all available satellites, RBSP-A was in the closest conjunction with FIREBIRD-II, despite the ~1.6 MLT difference. Therefore, we adopt the plasma and wave observations from RBSP-A (averaged over 02:37–02:42 UT around the FU3 conjunction) to determine which waves (among plasmaspheric hiss, MS waves, and EMIC waves) were primarily driving the electron precipitation, assuming that the wave and plasma conditions (near the equator) at the perfectly conjugate location to FIREBIRD are similar to those at the location of RBSP-A. The ratio of plasma frequency and electron gyrofrequency (f_{pe}/f_{ce}) is ~22.9. The EMIC wave spectrum used in the simulation has lower cutoffs of 0.26 f_{ci} (i: H and He), and upper cutoffs of 0.99 f_{cHe} for He-band and 0.65 f_{cH} for H-band, by only considering the wave power well above the background noise level ($>10^{-2}$ nT^2/Hz). EMIC waves are assumed to be field-aligned (consistent with the observations by RBSP-A), which leads to similar results by using the latitudinally varying wave normal distribution (Ni et al., 2015). We estimated the cold ion composition as 84%:3%:13% (H^+:He^+:O^+) by calculating the ion density from the two lowest HOPE channels following the method used in Blum et al. (2019) and Gamayunov et al. (2018).

Figures 4a–4c show the bounce-averaged pitch angle diffusion coefficients for EMIC waves at L ~ 5.9, calculated from cold plasma quasi-linear theory (Ni et al., 2015; Summers, 2005). The diffusion coefficients of hiss and MS waves are shown in Figure S3 in the supporting information. The diffusion coefficients for EMIC waves are higher than hiss and MS waves at energies above several hundred keV, indicating that EMIC waves dominated the pitch angle scattering and primarily drove the observed electron precipitation. While He-band EMIC waves efficiently scatter electrons at >~1 MeV at rates $>10^{-3}$ s^{-1} (Figure 4a), H-band ones scatter sub–MeV electrons at >~800 keV (Figure 4b).

Cold plasma theory may become invalid at frequencies close to f_{cHe}, where the He-band EMIC waves are strong (Figure 2g). Therefore, we also adopt a wavenumber analysis (Chen et al., 2019), which contains the physics of hot plasma, based only on the electromagnetic wave field data to extract the

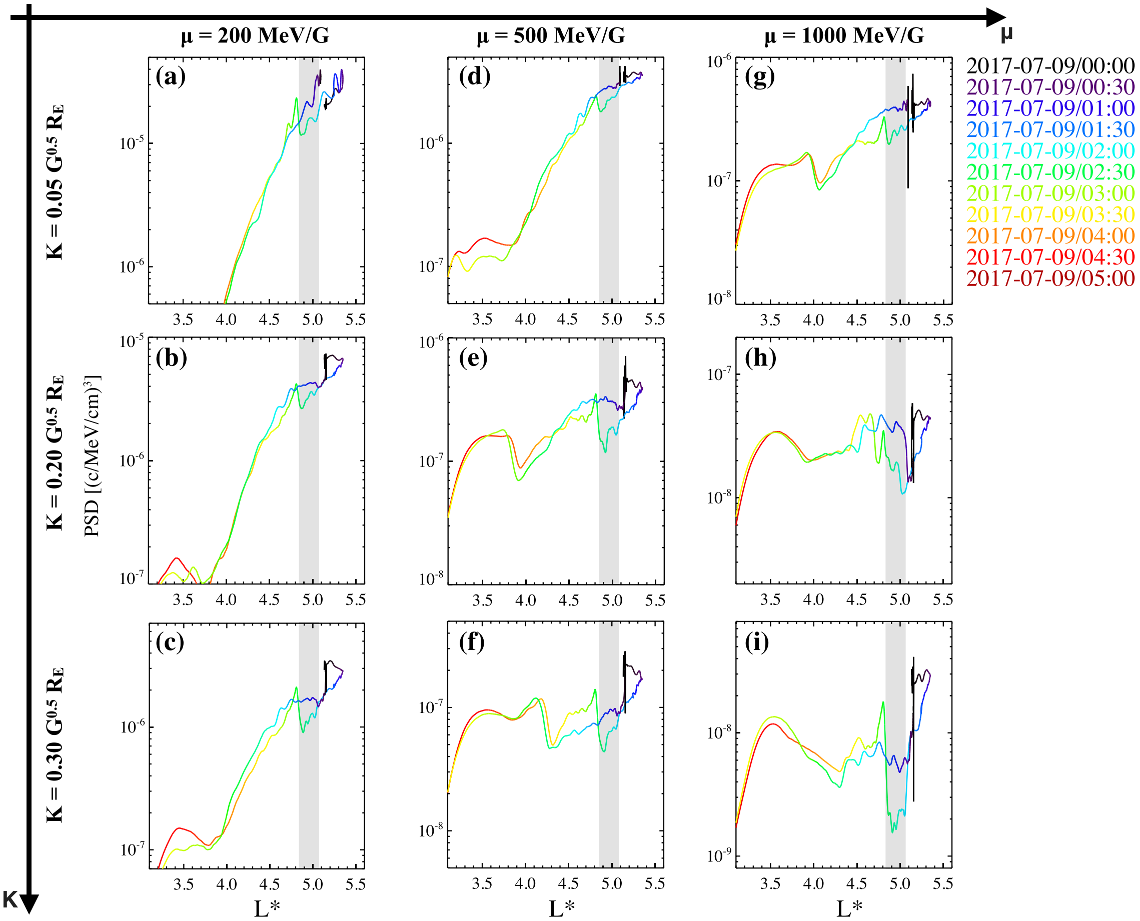

Figure 3. Evolution of electron phase space density (PSD) as a function of L* (T05). Columns (rows) show the PSD at constant values of the first (second) adiabatic invariant μ (K) with varying values of the second (first) adiabatic invariant K (μ). PSD is color coded every 30 min. Vertical gray blocks highlight the PSD dips.

wavenumber spectrum, where background plasma approximations or dispersion relation assumptions are not required. Two of the Maxwell's equations for the components of the electromagnetic fields are solved in the frequency domain (for details, see Chen et al., 2019) to obtain the median wavenumber spectrum (Figure 4g, black). After performing a power law fit to the obtained wave dispersion (Figure 4g, gray) and assuming constant wavenumber spectrum along the field line, it is possible to calculate the bounce-averaged pitch angle diffusion coefficients (Figures 4d–4f) and the minimum resonant energy (Figure 4h) for the observed parallel EMIC waves. As expected from hot plasma effects, He-band $E_{\min}$ increases (to ~4 MeV) compared to that predicted by the cold plasma calculation. Although the wavenumber spectrum shows high refractive index (kc/ω) in the H-band, lowering the hot plasma $E_{\min}$ down to ~700 keV, H-band EMIC waves can scatter electrons efficiently ($>10^{-3}$ s^{-1}) only at >~1 MeV.

In order to evaluate the scattering efficiency of each wave type, we compare the diffusion coefficients at the bounce loss cone to the strong diffusion limit (Figure 4i). We define electrons subject to "efficient pitch angle scattering" if their pitch angle diffusion coefficient is larger than 0.1 D_{SD}, where D_{SD} is the strong diffusion limit. With this definition, the minimum energy of electrons subject to efficient pitch angle scattering due to EMIC waves is ~800 keV (~1 MeV) for the results without (with) hot plasma effects included. Pitch angle scattering due to hiss and MS waves is well below the strong diffusion limit. All above findings indicate that H-band (He-band) EMIC waves play a dominant role in scattering electrons at energies ~0.8–4 MeV (>4 MeV) into the loss cone, suggesting that other mechanisms are required to precipitate electrons at <~800 keV.

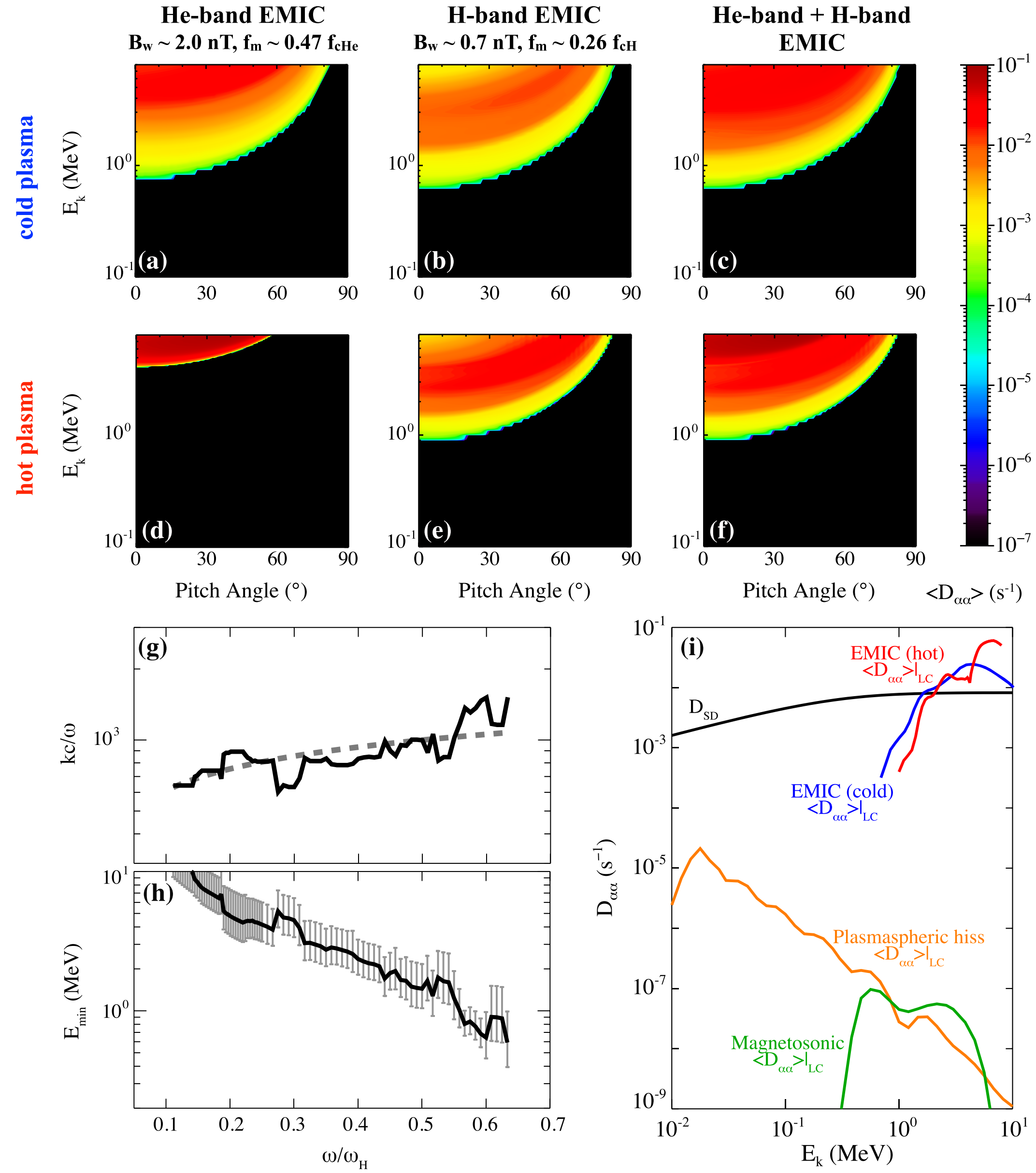

Figure 4. Bounce-averaged pitch angle diffusion coefficients without (a–c) and with (d–f) including hot plasma effects: He-band (a, d), H-band (b, e), and total EMIC waves (c, f). B_{W} is the root-mean-square wave amplitude during the EMIC wave interval 02:37–02:42 UT and f_{m} is the frequency corresponding to the highest EMIC wave intensity. (g) Median (black) and fit (dashed gray) of the wave refractive index from the wavenumber analysis and (h) median E_{min} with the first and third quartiles (gray vertical bars) versus normalized frequency. (i) Comparison between the strong diffusion limit (black) and the diffusion coefficients at the bounce loss cone color coded by each wave mode.

5. Summary and Discussion

In this letter, we report a direct observation of subrelativistic electron precipitation from FIREBIRD-II, potentially driven by EMIC waves. The principal findings of this study are summarized as follows.

1. Both FIREBIRD-II units observed electron precipitation from subrelativistic energies of ~250 keV up to ~1 MeV, strongest within L (T89) ~5.4–5.7 at ~17.9 MLT lasting at least ~11 min.
2. Near the time interval and location of precipitation, multipoint measurements from satellites and ground-based magnetometers recorded strong EMIC wave activity and EMIC-driven precipitation signatures. Among them, RBSP-A (the closest to FIREBIRD-II, albeit with ΔMLT ~ 1.6) observed intense He-band waves (B_w ~ 2.0 nT) and modest H-band waves (B_w ~ 0.7 nT). NOAA-18 and NOAA-19, crossing

similar L shells at MLTs between FIREBIRD and RBSP-A, observed ~ 10s–100s keV proton precipitation as well, a typical signature of EMIC-driven precipitation.

3. Simultaneously with EMIC waves, plasmaspheric hiss and MS waves were also observed by RBSP-A, although much weaker (8 and 37 pT, respectively). The calculation of the quasi-linear pitch angle diffusion coefficients indicates that while hiss and MS waves did not scatter electrons efficiently, H-band (He-band) EMIC waves played a major role in driving the electron precipitation at energies ~0.8–4 MeV (>4 MeV).
4. The EMIC waves observed by RBSP-A over ~02:30–03:00 UT were also associated with electron flux dropouts in the outer radiation belt. The PSD profiles revealed by RBSP indeed show localized dips coincident with EMIC waves, which become more evident as μ and K increase. Interestingly, the PSD dips were evident at relatively low values of μ, indicating that EMIC waves played a role in precipitating radiation belt electrons even at a few 100s keV. The scale size and location of PSD dips agree well with the L shell extent of EMIC waves and electron precipitation measured by FIREBIRD-II.

It is important to note that the simulation results without (with) including hot plasma effects due to EMIC waves can only explain the electron precipitation at energies >~800 keV (>~1 MeV), requiring other mechanisms to explain the low energy electron precipitation down to ~250 keV. For example, nonresonant scattering (e.g., Chen et al., 2016) and nonlinear effects (Denton et al., 2019; Hendry et al., 2019; Kubota et al., 2015; Omura & Zhao, 2012, 2013) are suggested to lower the E_{min} down to a few 100s keV. However, the evaluation of these effects is beyond the scope of this case study and left as future investigation.

The results of our study are consistent with previous observations of sub–MeV electron precipitation (e.g., Capannolo et al., 2019; Clilverd et al., 2015; Hendry et al., 2017). However, the differential energy channels extending down to ~250 keV, available on FIREBIRD-II, allowed us to directly and unambiguously detect subrelativistic electron precipitation without further assumptions or modeling, and without proton contamination, which has been limiting reliable observations from POES at subrelativistic energies. Owing to a combination of multiple satellites and ground-based stations, our study provides the direct observation of subrelativistic (at least down to ~250 keV) electron precipitation due to efficient pitch angle scattering potentially driven by the observed EMIC waves as summarized in (1)–(4), although quasi-linear theory is insufficient to explain the full precipitation energy range and no wave measurements were available at the exact conjugate location to FIREBIRD. Nevertheless, this case study highlights FIREBIRD-II capabilities to provide electron measurements with high resolution in time and energy not only for microbursts but also for other precipitation patterns, such as EMIC-driven electron precipitation, and also potentially provide a valuable interpretation of electron precipitation data from POES and other LEO satellites.

Acknowledgments
This research is supported by NSF Grants AGS-1723588 and AGS-1847818, AFOSR Grant FA9550-15-1-0158, and the Alfred P. Sloan Research Fellowship FG-2018-10936. The Van Allen probes data from the EMFISIS instrument suite were obtained from http://emfisis.physics.uiowa.edu/Flight/, and data from the ECT instrument were obtained from the website (http://www.rbsp-ect.lanl.gov/data_pub/). The POES data are available at the https://www.ngdc.noaa.gov/stp/satellite/poes/ website. We thank Yukitoshi Nishimura for checking other proton precipitation observations and Anthony Saikin for the useful discussion on radiation belt losses during this event. We acknowledge the World Data Center for Geomagnetism, Kyoto for providing the AL index (http://wdc.kugi.kyoto-u.ac.jp/kp/index.html). FIREBIRD data (accessible at http://solar.physics.montana.edu/FIREBIRD_II/) was made possible by the NSF Grants: 0838034 and 1339414. GOES magnetometer data are accessible at the website (https://www.ngdc.noaa.gov/stp/satellite/goes/dataaccess.html). The authors thank the CARISMA team for data (accessible at http://carisma.ca/carisma-data-repository and http://data.carisma.ca). CARISMA is operated by the University of Alberta, funded by the Canadian Space Agency. The Athabasca magnetometer is operated by ERG (Exploration of energization and Radiation in Geospace) Science Center in collaboration with the Athabasca University (data accessible at https://ergsc.isee.nagoya-u.ac.jp/data/ergsc/ground/geomag/isee/induction/); we thank Prof. Martin Connors for supporting operation of the induction coils at Athabasca University Geospace Observatory, a facility supported by the Canada Foundation for Innovation. Work at UTD was supported by the NASA grants 80NSSC19K0282 and 80NSSC19K0283, and the AFOSR grant of FA9550-16-1-0344.

References

Allen, R. C., Zhang, J.-C., Kistler, L. M., Spence, H. E., Lin, R.-L., Klecker, B., et al. (2016). A statistical study of EMIC waves observed by Cluster: 2. Associated plasma conditions. *Journal of Geophysical Research: Space Physics*, *121*, 6458–6479. https://doi.org/10.1002/2016JA022541

Blum, L. W., Artemyev, A., Agapitov, O., Mourenas, D., Boardsen, S., & Schiller, Q. (2019). EMIC wave-driven bounce resonance scattering of energetic electrons in the inner magnetosphere. *Journal of Geophysical Research: Space Physics*, *124*. https://doi.org/10.1029/2018JA026427

Blum, L. W., Bonnell, J. W., Agapitov, O., Paulson, K., & Kletzing, C. (2017). EMIC wave scale size in the inner magnetosphere: Observations from the dual Van Allen Probes. *Geophysical Research Letters*, *44*, 1227–1233. https://doi.org/10.1002/2016GL072316

Blum, L. W., Halford, A., Millan, R., Bonnell, J. W., Goldstein, J., Usanova, M., et al. (2015). Observations of coincident EMIC wave activity and duskside energetic electron precipitation on 18–19 January 2013. *Geophysical Research Letters*, *42*, 5727–5735. https://doi.org/10.1002/2015GL065245

Breneman, A. W., Crew, A., Sample, J., Klumpar, D., Johnson, A., Agapitov, O., & Kletzing, C. A. (2017). Observations directly linking relativistic electron microbursts to whistler mode chorus: Van Allen Probes and FIREBIRD II. *Geophysical Research Letters*, *44*, 11,265–11, 272. https://doi.org/10.1002/2017GL075001

Cao, X., Ni, B., Liang, J., Xiang, Z., Wang, Q., Shi, R., et al. (2016). Resonant scattering of central plasma sheet protons by multiband EMIC waves and resultant proton loss timescales. *Journal of Geophysics Research: Space Physics*, *121*, 1219–1232. https://doi.org/10.1002/2015JA021933

Capannolo, L., Li, W., Ma, Q., Shen, X.-C., Zhang, X.-J., Redmon, R. J., et al. (2019). Energetic electron precipitation: Multievent analysis of its spatial extent during EMIC wave activity. *Journal of Geophysical Research: Space Physics*, *124*. https://doi.org/10.1029/2018JA026291

Capannolo, L., Li, W., Ma, Q., Zhang, X.-J., Redmon, R. J., Rodriguez, J. V., et al. (2018). Understanding the driver of energetic electron precipitation using coordinated multisatellite measurements. *Geophysical Research Letters*, *45*, 6755–6765. https://doi.org/10.1029/2018GL078604

Chen, L., Thorne, R. M., & Bortnik, J. (2011). The controlling effect of ion temperature on EMIC wave excitation and scattering. *Geophysical Research Letters*, *38*, L16109. https://doi.org/10.1029/2011GL048653

Chen, L., Thorne, R. M., Bortnik, J., & Zhang, X.-J. (2016). Nonresonant interactions of electromagnetic ion cyclotron waves with relativistic electrons. *Journal of Geophysics Research: Space Physics*, *121*, 9913–9925. https://doi.org/10.1002/2016JA022813

Chen, L., Zhu, H., & Zhang, X. (2019). Wavenumber analysis of EMIC waves. *Geophysical Research Letters*, *46*, 5689–5697. https://doi.org/10.1029/2019GL082686

Chen, Y., Friedel, R. H. W., & Reeves, G. D. (2006). Phase space density distributions of energetic electrons in the outer radiation belt during two Geospace Environment Modeling Inner Magnetosphere/Storms selected storms. *Journal of Geophysical Research*, *111*, A11S04. https://doi.org/10.1029/2006JA011703

Clilverd, M. A., Duthie, R., Hardman, R., Hendry, A. T., Rodger, C. J., Raita, T., et al. (2015). Electron precipitation from EMIC waves: A case study from 31 May 2013. *Journal of Geophysical Research: Space Physics*, *120*, 3618–3631. https://doi.org/10.1002/2015JA021090

Crew, A., Spence, H. E., Blake, J. B., Klumpar, D. M., Larsen, B. A., O'Brien, T. P., et al. (2016). First multipoint in situ observations of electron microbursts: Initial results from the NSF FIREBIRD-II mission. *Journal of Geophysical Research: Space Physics*, *121*, 5272–5283. https://doi.org/10.1002/2016JA022485

Denton, R. E., Ofman, L., Shprits, Y. Y., Bortnik, J., Millan, R. M., Rodger, C. J., et al. (2019). Pitch angle scattering of sub-MeV relativistic electrons by electromagnetic ion cyclotron waves. *Journal of Geophysical Research: Space Physics*, *124*, 5610–5626. https://doi.org/10.1029/2018JA026384

Engebretson, M. J., Lessard, M. R., Bortnik, J., Green, J. C., Horne, R. B., Detrick, D. L., et al. (2008). Pc1–Pc2 waves and energetic particle precipitation during and after magnetic storms: Superposed epoch analysis and case studies. *Journal of Geophysical Research*, *113*, A01211. https://doi.org/10.1029/2007JA012362

Engebretson, M. J., Posch, J. L., Braun, D. J., Li, W., Ma, Q., Kellerman, A. C., et al. (2018). EMIC wave events during the four GEM QARBM challenge intervals. *Journal of Geophysical Research: Space Physics*, *123*, 6394–6423. https://doi.org/10.1029/2018JA025505

Engebretson, M. J., Posch, J. L., Wygant, J. R., Kletzing, C. A., Lessard, M. R., Huang, C. L., et al. (2015). Van Allen probes, NOAA, GOES, and ground observations of an intense EMIC wave event extending over 12 h in magnetic local time. *Journal of Geophysical Research: Space Physics*, *120*, 5465–5488. https://doi.org/10.1002/2015JA021227

Erlandson, R. E., & Ukhorskiy, A. J. (2001). Observations of electromagnetic ion cyclotron waves during geomagnetic storms: Wave occurrence and pitch angle scattering. *Journal of Geophysical Research*, *106*(A3), 3883–3895. https://doi.org/10.1029/2000JA000083

Fraser, B. J., Grew, R. S., Morley, S. K., Green, J. C., Singer, H. J., Loto'aniu, T. M., & Thomsen, M. F. (2010). Storm time observations of electromagnetic ion cyclotron waves at geosynchronous orbit: GOES results. *Journal of Geophysics Research*, *115*, A05208. https://doi.org/10.1029/2009JA014516

Funsten, H. O., Skoug, R. M., Guthrie, A. A., MacDonald, E. A., Baldonado, J. R., Harper, R. W., et al. (2013). Helium, Oxygen, Proton, and Electron (HOPE) Mass Spectrometer for the Radiation Belt Storm Probes Mission. *Space Science Reviews*, *179*(1-4), 423–484. https://doi.org/10.1007/s11214-013-9968-7

Gamayunov, K. V., Min, K., Saikin, A. A., & Rassoul, H. (2018). Generation of EMIC waves observed by Van Allen Probes at low L shells. *Journal of Geophysical Research: Space Physics*, *123*, 8533–8556. https://doi.org/10.1029/2018JA025629

Greeley, A. D., Kanekal, S. G., Baker, D. N., Klecker, B., & Schiller, Q. (2019). Quantifying the contribution of microbursts to global electron loss in the radiation belts. *Journal of Geophysical Research: Space Physics*, *124*, 1111–1124. https://doi.org/10.1029/2018JA026368

Hendry, A. T., Rodger, C. J., & Clilverd, M. A. (2017). Evidence of sub-MeV EMIC-driven electron precipitation. *Geophysical Research Letters*, *44*, 1210–1218. https://doi.org/10.1002/2016GL071807

Hendry, A. T., Santolík, O., Kletzing, C. A., Rodger, C. J., Shiokawa, K., & Baishev, D. (2019). Multi-instrument observation of nonlinear EMIC-driven electron precipitation at sub–MeV energies. *Geophysical Research Letters*, *46*, 7248–7257. https://doi.org/10.1029/2019GL082401

Hirai, A., Tsuchiya, F., Obara, T., Kasaba, Y., Katoh, Y., Misawa, H., et al. (2018). Temporal and spatial correspondence of Pc1/EMIC waves and relativistic electron precipitations observed with ground-based multi-instruments on 27 March 2017. *Geophysical Research Letters*, *45*(24), 13,182–13,191. https://doi.org/10.1029/2018GL080126

Jordanova, V. K., Albert, J., & Miyoshi, Y. (2008). Relativistic electron precipitation by EMIC waves from self-consistent global simulations. *Journal of Geophysics Research*, *113*, A00A10. https://doi.org/10.1029/2008JA013239

Jordanova, V. K., & Miyoshi, Y. S. (2005). Relativistic model of ring current and radiation belt ions and electrons: Initial results. *Geophysical Research Letters*, *32*, L14104. https://doi.org/10.1029/2005GL023020

Kim, H., Lessard, M. R., Engebretson, M. J., & Lühr, H. (2010). Ducting characteristics of Pc 1 waves at high latitudes on the ground and in space. *Journal of Geophysical Research*, *115*, A09310. https://doi.org/10.1029/2010JA015323

Kletzing, C. A., Kurth, W. S., Acuna, M., MacDowall, R. J., Torbert, R. B., Averkamp, T., et al. (2013). The Electric and Magnetic Field Instrument Suite and Integrated Science (EMFISIS) on RBSP. *Space Science Reviews*, *179*(1-4), 127–181. https://doi.org/10.1007/s11214-013-9993-6

Klumpar, D., L. Springer, E. Mosleh, K. Mashburn, S. Berardinelli, A. Gunderson, et al. (2015), Flight system technologies enabling the twin-CubeSat FIREBIRD-II scientific mission, *Proceedings of the 29thAnnual AIAA/USU Conference on Small Satellites, Technical Section V: Year in Review*, SSC15-V-6, http://digitalcommons.usu.edu/smallsat/2015/all2015/35/.

Kubota, Y., Omura, Y., & Summers, D. (2015). Relativistic electron precipitation induced by EMIC-triggered emissions in a dipole magnetosphere. *Journal of Geophysical Research: Space Physics*, *120*, 4384–4399. https://doi.org/10.1002/2015JA021017

Kurth, W. S., De Pascuale, S., Faden, J. B., Kletzing, C. A., Hospodarsky, G. B., Thaller, S., & Wygant, J. R. (2015). Electron densities inferred from plasma wave spectra obtained by the Waves instrument on Van Allen Probes. *Journal of Geophysical Research: Space Physics*, *120*, 904–914. https://doi.org/10.1002/2014JA020857

Li, W., Shprits, Y. Y., & Thorne, R. M. (2007). Dynamic evolution of energetic outer zone electrons due to wave-particle interactions during storms. *Journal of Geophysics Research*, *112*, A10220. https://doi.org/10.1029/2007JA012368

Mann, I. R., Milling, D. K., Rae, I. J., Ozeke, L. G., Kale, A., Kale, Z. C., et al. (2008). The upgraded CARISMA magnetometer array in the THEMIS era. *Space Science Reviews*, *141*(1-4), 413–451. https://doi.org/10.1007/s11214-008-9457-6

Mauk, B. H., Fox, N. J., Kanekal, S. G., Kessel, R. L., Sibeck, D. G., & Ukhorskiy, A. (2013). Science objectives and rationale for the Radiation Belt Storm Probes Mission. *Space Science Reviews*, *179*(1-4), 3–27. https://doi.org/10.1007/s11214-012-9908-y

Meraner, K., & Schmidt, H. (2018). Climate impact of idealized winter polar mesospheric and stratospheric ozone losses as caused by energetic particle precipitation. *Atmospheric Chemistry and Physics*, *18*, 1079–1089. https://doi.org/10.5194/acp-18-1079-2018

Meredith, N. P., Horne, R. B., Kersten, T., Fraser, B. J., & Grew, R. S. (2014). Global morphology and spectral properties of EMIC waves derived from CRRES observations. *Journal of Geophysics Research: Space Physics*, *119*, 5328–5342. https://doi.org/10.1002/2014JA020064

Meredith, N. P., Thorne, R. M., Horne, R. B., Summers, D., Fraser, B. J., & Anderson, R. R. (2003). Statistical analysis of relativistic electron energies for cyclotron resonance with EMIC waves observed on CRRES. *Journal of Geophysical Research*, *108*(A6), 1250. https://doi.org/10.1029/2002JA009700

Min, K., Lee, J., Keika, K., & Li, W. (2012). Global distribution of EMIC waves derived from THEMIS observations. *Journal of Geophysics Research*, *117*, A05219. https://doi.org/10.1029/2012JA017515

Miyoshi, Y., Sakaguchi, K., Shiokawa, K., Evans, D., Albert, J., Connors, M., & Jordanova, V. (2008). Precipitation of radiation belt electrons by EMIC waves, observed from ground and space. *Geophysical Research Letters*, *35*, L23101. https://doi.org/10.1029/2008GL035727

Ni, B., Cao, X., Zou, Z., Zhou, C., Gu, X., Bortnik, J., et al. (2015). Resonant scattering of outer zone relativistic electrons by multiband EMIC waves and resultant electron loss time scales. *Journal of Geophysical Research: Space Physics*, *120*, 7357–7373. https://doi.org/10.1002/2015JA021466

Omura, Y., & Zhao, Q. (2012). Nonlinear pitch angle scattering of relativistic electrons by EMIC waves in the innermagnetosphere. *Journal of Geophysical Research*, *117*, A08227. https://doi.org/10.1029/2012JA017943

Omura, Y., & Zhao, Q. (2013). Relativistic electron microbursts due to nonlinear pitch angle scattering by EMIC triggered emissions. *Journal of Geophysical Research: Space Physics*, *118*, 5008–5020. https://doi.org/10.1002/jgra.50477

Peck, E. D., Randall, C. E., Green, J. C., Rodriguez, J. V., & Rodger, C. J. (2015). POES MEPED differential flux retrievals and electron channel contamination correction. *Journal of Geophysics Research: Space Physics*, *120*, 4596–4612. https://doi.org/10.1002/2014JA020817

Qin, M., Hudson, M., Li, Z., Millan, R., Shen, X., Shprits, Y., et al. (2019). Investigating loss of relativistic electrons associated with EMIC waves at low L values on 22 June 2015. *Journal of Geophysical Research: Space Physics*, *124*. https://doi.org/10.1029/2018JA025726

Qin, M., Hudson, M., Millan, R., Woodger, L., & Shekhar, S. (2018). Statistical investigation of the efficiency of EMIC waves in precipitating relativistic electrons. *Journal of Geophysical Research: Space Physics*, *123*(8), 6223–6230. https://doi.org/10.1029/2018JA025419

Shekhar, S., Millan, R., & Smith, D. (2017). A statistical study of the spatial extent of relativistic electron precipitation with polar orbiting environmental satellites. *Journal of Geophysical Research: Space Physics*, *122*, 11,274–11,284. https://doi.org/10.1002/2017JA024716

Shprits, Y. Y., Kellerman, A., Aseev, N., Drozdov, A. Y., & Michaelis, I. (2017). Multi-MeV electron loss in the heart of the radiation belts. *Geophysical Research Letters*, *44*, 1204–1209. https://doi.org/10.1002/2016GL072258

Shumko, M., Sample, J., Johnson, A., Blake, J. B., Crew, A. B., Spence, H. E., et al. (2018). Microburst scale size derived from multiple bounces of a microburst simultaneously observed with the FIREBIRD-II CubeSats,II CubeSats. *Geophysical Research Letters*, *45*, 8811–8818. https://doi.org/10.1029/2018GL078925

Spence, H. E., Blake, J. B., Crew, A. B., Driscoll, S., Klumpar, D. M., Larsen, B. A., et al. (2012). Focusing on size and energy dependence of electron microbursts from the Van Allen Radiation Belts. *Space Weather*, *10*, S11004. https://doi.org/10.1029/2012SW000869

Spence, H. E., Reeves, G. D., Baker, D. N., Blake, J. B., Bolton, M., Bourdarie, S., et al. (2013). Science goals and overview of the Radiation Belt Storm Probes (RBSP) Energetic Particle, Composition, and Thermal Plasma (ECT) Suite on NASA's Van Allen Probes Mission. *Space Science Reviews*, *179*(1-4), 311–336. https://doi.org/10.1007/s11214-013-0007-5

Su, Z., Gao, Z., Zhu, H., Li, W., Zheng, H., Wang, Y., et al. (2016). Nonstorm time dropout of radiation belt electron fluxes on 24 September 2013. *Journal of Geophysics Research: Space Physics*, *121*, 6400–6416. https://doi.org/10.1002/2016JA022546

Summers, D. (2005). Quasi-linear diffusion coefficients for field-aligned electromagnetic waves with applications to the magnetosphere. *Journal of Geophysics Research*, *110*, A08213. https://doi.org/10.1029/2005JA011159

Summers, D., Shi, R., Engebretson, M. J., Oksavik, K., Manweiler, J. W., & Mitchell, D. G. (2017). Energetic proton spectra measured by the Van Allen Probes. *Journal of Geophysical Research: Space Physics*, *122*, 10,129–10,144. https://doi.org/10.1002/2017JA024484

Summers, D., & Thorne, R. M. (2003). Relativistic electron pitch-angle scattering by electromagnetic ion cyclotron waves during geomagnetic storms. *Journal of Geophysics Research*, *108*(A4), 1143. https://doi.org/10.1029/2002JA009489

Tsyganenko, N. A. (1989). A solution of the Chapman-Ferraro problem for an ellipsoidal magnetopause. *Planetary and Space Science*, *37*(9), 1037–1046. https://doi.org/10.1016/0032-0633(89)90076-7

Tsyganenko, N. A., & Sitnov, M. I. (2005). Modeling the dynamics of the inner magnetosphere during strong geomagnetic storms. *Journal of Geophysics Research*, *110*, A03208. https://doi.org/10.1029/2004JA010798

Usanova, M. E., Drozdov, A., Orlova, K., Mann, I. R., Shprits, Y., Robertson, M. T., et al. (2014). Effect of EMIC waves on relativistic and ultrarelativistic electron populations: Ground-based and Van Allen Probes observations. *Geophysical Research Letters*, *41*, 1375–1381. https://doi.org/10.1002/2013GL059024

Woodger, L. A., Millan, R. M., Li, Z., & Sample, J. G. (2018). Impact of background magnetic field for EMIC wave-driven electron precipitation. *Journal of Geophysical Research: Space Physics*, *123*, 8518–8532. https://doi.org/10.1029/2018JA025315

Xiang, Z., Tu, W., Li, X., Ni, B., Morley, S. K., & Baker, D. N. (2017). Understanding the mechanisms of radiation belt dropouts observed by Van Allen Probes. *Journal of Geophysical Research: Space Physics*, *122*, 9858–9879. https://doi.org/10.1002/2017JA024487

Yuan, Z., Deng, X., Lin, X., Pang, Y., Zhou, M., Décréau, P. M. E., et al. (2010). Link between EMIC waves in a plasmaspheric plume and a detached sub-auroral proton arc with observations of Cluster and IMAGE satellites. *Geophysical Research Letters*, *37*, L07108. https://doi.org/10.1029/2010GL042711

Yuan, Z., Liu, K., Yu, X., Yao, F., Huang, S., Wang, D., & Ouyang, Z. (2018). Precipitation of radiation belt electrons by EMIC waves with conjugated observations of NOAA and Van Allen satellites. *Geophysical Research Letters*, *45*, 12,694–12,702. https://doi.org/10.1029/2018GL080481

References From the Supporting Information

Carson, B. R., Rodger, C. J., & Clilverd, M. A. (2013). POES satellite observations of EMIC-wave driven relativistic electron precipitation during 1998–2010. *Journal of Geophysical Research: Space Physics*, *118*, 232–243. https://doi.org/10.1029/2012JA017998

Gilson, M. L., Raeder, J., Donovan, E., Ge, Y. S., & Kepko, L. (2012). Global simulation of proton precipitation due to field line curvature during substorms. *Journal of Geophysical Research*, *117*, A05216. https://doi.org/10.1029/2012JA017562

Green, J. C. (2013), MEPED Telescope Data Processing Algorithm Theoretical Basis Document, Natl. Oceanic and Atmos. Admin. National Geophysical Data Center, Boulder, Colo.

Rodger, C. J., Clilverd, M. A., Green, J. C., & Lam, M. M. (2010). Use of POES SEM-2 observations to examine radiation belt dynamics and energetic electron precipitation into the atmosphere. *Journal of Geophysics Research*, *115*, A04202. https://doi.org/10.1029/2008JA014023

Yahnin, A. G., Yahnina, T. A., Raita, T., & Manninen, J. (2017). Ground pulsation magnetometer observations conjugated with relativistic electron precipitation. *Journal of Geophysics Research: Space Physics*, *122*, 9169–9182. https://doi.org/10.1002/2017JA024249

Yahnin, A. G., Yahnina, T. A., Semenova, N. V., Gvozdevsky, B. B., & Pashin, A. B. (2016). Relativistic electron precipitation as seen by NOAA POES. *Journal of Geophysics Research: Space Physics*, *121*, 8286–8299. https://doi.org/10.1002/2016JA022765

Yando, K., Millan, R. M., Green, J. C., & Evans, D. S. (2011). A Monte Carlo simulation of the NOAA POES Medium Energy Proton and Electron Detector instrument. *Journal of Geophysics Research*, *116*, A10231. https://doi.org/10.1029/2011JA016671

Erratum

Due to a production error, an outdated version of Figure 2 appeared in the originally published version of this article. This error has been corrected, and the present version may be considered the official version of record.